Population of high spin states by quasi-elastic and deep inelastic collisions

H. Takai, C. N. Knott, D. F. Winchell, J. X. Saladin, M. S. Kaplan, and L. de Faro
Department of Physics, University of Pittsburgh, Pittsburgh, Pennsylvania 15260

R. Aryaeinejad, R. A. Blue, R. M. Ronningen, and D. J. Morrissey
National Superconducting Cyclotron Laboratory, Michigan State University, East Lansing, Michigan 48824

I. Y. Lee
Oak Ridge National Laboratory, Oak Ridge, Tennessee 37831

O. Dietzsch
Instituto de Fisica, Universidade de Saõ Paulo, Caixa Postal 20516, Saõ Paulo, Brazil
(Received 4 April 1988)

The feasibility of populating high spin states using reactions induced by a 10 MeV/nucleon ^{22}Ne beam on ^{170}Er was studied. The experiment was carried out using a multidetector array for high resolution γ-ray spectroscopy, a 14 element sum-multiplicity spectrometer and six ΔE-E telescopes. Detailed information was obtained concerning the reaction mechanisms associated with various reaction channels. Deep inelastic collisions are shown to be a promising tool for high spin spectroscopy in regions of the chart of nuclides which are not accessible by other reactions.

I. INTRODUCTION

In the past, high spin states in nuclei have been studied primarily through the use of fusion evaporation reactions[1] induced by heavy ions. This type of reaction is well understood and can be used to create compound systems with a large amount of angular momentum (up to $100\hbar$). Due to the nature of the reaction, some nucleon and/or α evaporation takes place until the system becomes stable with respect to particle (primarily neutron) emission. Because of this, it is not possible to study high spin states in neutron-rich nuclei using this type of reaction.

Recently, Guidry *et al.*[2] have demonstrated that high spins states in neutron-rich nuclei can be populated using transfer reactions induced by heavy projectiles (Ni,Sn) at bombarding energies slightly above the Coulomb barrier. In this type of reaction, the final nucleus receives a significant fraction of its angular momentum via multiple Coulomb excitation before and after the nucleon transfer takes place.

Here we present the results of the reaction ^{22}Ne+^{170}Er at a bombarding energy of 10 MeV/nucleon, which corresponds to about twice the Coulomb barrier energy. The purpose of the experiment was to study in detail the reaction mechanisms associated with various exit channels, in order to assess the usefulness of such reactions for the study of high spin states. On the basis of extensive previous work,[3-6] one expects the dominant reaction mechanisms to be quasi-elastic collisions, including incomplete fusion, massive transfer or "breakup" fusion, and deep inelastic collisions (DIC). One anticipates, particularly in the case of DIC, a significant amount of the orbital angular momentum between the projectile and the target to be converted into high spin excitation. The high value of the angular momentum brought to the system is reflected in the observed high multiplicity of γ rays.[7,8] Quasi-elastic reactions (QE) at these energies are predominantly governed by transfers of nucleons that can range from few nucleons up to massive clusters (e.g., ^{5}He,^{6}He) and also by possible breakup channels.[9] The transfer of such neutron-rich clusters can be attractive technique to populate high spin states in nuclei on the neutron-rich side of the valley of stability.

In the present experiment, both types of reaction mechanisms, quasi-elastic and DIC, were investigated using an array containing γ-ray and particle detectors, allowing identification of both the targetlike fragment (TLF) and projectilelike fragment (PLF) in a given reaction. Both PLF-γ and γ-γ coincidence events were collected.

II. EXPERIMENTAL

Enriched (99%) ^{170}Er targets of thickness 1 mg/cm^2 were bombarded with a 220-MeV ^{22}Ne beam obtained from the K-500 Superconducting Cyclotron at Michigan State University. The target was mounted at 55° with respect to the beam direction and a shielded Faraday cup was used to measure the beam current incident on the target. The average beam current was about 20–30 charge nA.

To detect both γ rays and ejectiles, the Pittsburgh Multidetector Array[10] was used together with six silicon E-ΔE telescopes. Figure 1 shows a schematic diagram of the apparatus. The γ-ray-detector array was composed of five high-purity, Compton-suppressed germanium (HPGe) detectors and a 14-element bismuth germanate (BGO) Sum Energy and Multiplicity Spectrometer (SMS). The Ge detectors in this experiment were placed at 72.3,

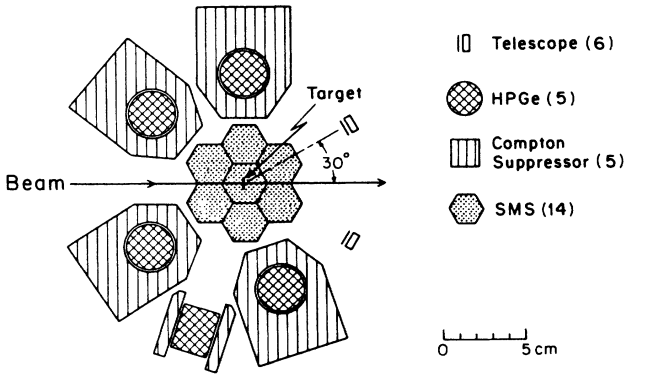

FIG. 1. Horizontal cross section of the apparatus showing the various types of detectors and their arrangement.

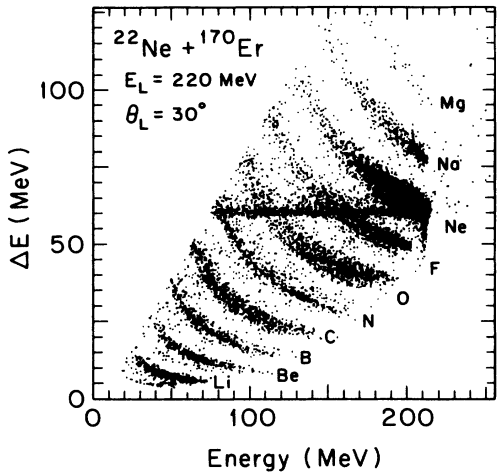

FIG. 2. ΔE vs E plot showing the Z identification of the PLF's. This plot does not have sufficient resolution to show the mass separation. The horizontal structure is related to the intense elastic peak and is due to the low energy tail that is associated with the detection of heavy ions in Si detectors.

92.3, 101.2, 142.2, and 145.0 degrees with respect to the beam direction. The SMS elements were distributed seven above and seven below the target chamber and covered a total solid angle of $\sim 30\%$ of 4π. The silicon telescopes were mounted at $\theta = 30°$ with respect to the beam direction, near the classical grazing angle for this reaction. The ΔE and E Si detectors had thicknesses of 74 and 500 μm, respectively. All telescopes were cooled to $-20\,°C$ in order to improve isotope resolution.

The energy resolution and the peak-to-total ratio (number of counts under the full energy peak, divided by the total number of counts) for the Ge detectors, measured with a ^{60}Co source, were about 2.5 KeV and 55%, respectively. The average resolution of the SMS elements was 15% for the 667-keV line of a ^{137}Cs source. The energy and efficiency calibration of the Ge detectors were carried out with ^{60}Co, ^{88}Y, ^{152}Eu, ^{182}Ta, and ^{22}Na radioactive sources in the target position. The mass separation obtained in the telescopes was one mass number at $A = 22$. Energy calibration of the telescopes was done using the elastic scattering peak and an ^{241}Am α source. The linearity was checked with a precision pulser. The solid angles of the germanium detectors were defined by heavy-metal collimators and averaged 25 msr. The solid angle for each telescope was 13 msr.

With this arrangement, two types of events, namely, particle-γ and γ-γ coincidences, were acquired. For particle-γ events, α particles and lighter ions were rejected. In either case, the energy and timing relative to the event trigger were recorded for each element of the SMS for later analysis. The data were recorded on magnetic tape event by event.

III. RESULTS AND DISCUSSION

A. General features of the data

The first step in the data analysis was to characterize different reaction mechanisms responsible for producing the many outgoing channels. In order to identify different PLF channels and to survey their degree of inelasticity, the data from the silicon telescopes were used in conjunction with the γ-ray multiplicity information from the SMS.

A resolution of about one mass unit for $A = 22$ was obtained with the surface barrier telescopes. This allowed us to identify PLF's from ^{6}Li to ^{24}Mg. Figure 2 shows a two-dimensional scatter plot of E vs ΔE for inclusive data (i.e., no γ coincidence requirement). Because of size limitations, this figure does not reveal the isotope resolution. The dominant exit channels are the elastic channel and the one- and two-neutron stripping channels, which account for about 48% of the total observed fragments. The figure also shows the predominance of "stripping" channels over "pickup" reactions. Inclusive relative yields for all exit channels, normalized to the elastic channel, are listed in Table I.

TABLE I. Column 2 lists the relative inclusive cross sections in percent of the elastic channel. The numbers in brackets represent the uncertainties in the last quoted digit.

Isotope	Relative yield
^{24}Na	0.26(3)
^{23}Na	1.9(2)
^{23}Ne	8.0(1)
^{22}Ne	100
^{21}Ne	7.0(1)
^{20}Ne	2.0(5)
^{21}F	3.5(4)
^{20}F	2.7(3)
^{19}F	1.9(2)
^{20}O	0.6(1)
^{19}O	1.4(2)
^{18}O	2.6(3)
^{17}O	1.7(2)
^{16}O	1.5(2)
^{17}N	0.49(7)
^{16}N	0.7(1)
^{15}N	2.3(3)
^{14}N	0.43(7)
^{13}C	1.7(2)
^{12}C	1.9(2)
^{11}C	1.5(2)

The evolution of the various reaction mechanisms as a function of the number of transferred protons and neutrons can best be seen from two-dimensional contour maps of the intensity as a function of fold (K) and PLF energy. These maps are shown in Fig. 3. The corresponding PLF energy spectra, i.e., the projections of these maps onto the PLF-energy axis, are shown in Fig. 4. Included in the latter are the spectra for some of the weaker channels for which we did not produce contour maps. Using standard calibration procedures, it is possible to derive from the fold the γ-ray multiplicity (M).[11,12] Both quantities are indicated in Fig. 3. It should be understood that K and M refer to the sum of the folds and multiplicities of cascades from the TLF and the PLF fragments.

For PLF's close to the projectile mass, one observes in each of Figs. 3 and 4 a well-defined maximum corresponding to quasi-elastic processes. This maximum broadens as more and more nucleons are transferred, and a sudden disappearance of the QE peak occurs when one moves from oxygen to nitrogen isotopes. The QE peak is not observed for any of the lighter ions ($Z \leq 7$), but the expected positions are indicated in Fig. 4 by arrows. Starting with ^{19}O, a second maximum appears at a considerably lower PLF energy, but with higher multiplicity, corresponding to DIC processes. The onset of DIC processes can already be observed in ^{19,20}F and ^{20}O through the appearance of a "plateau" in the region where DIC processes are expected. For the lightest PLF's (^{15}N, ^{12}C, and ^{11}B) one observes only the DIC maxima with a ridge extending towards the quasi-elastic region.

The positions of the maxima in the E_{PLF} vs M plane

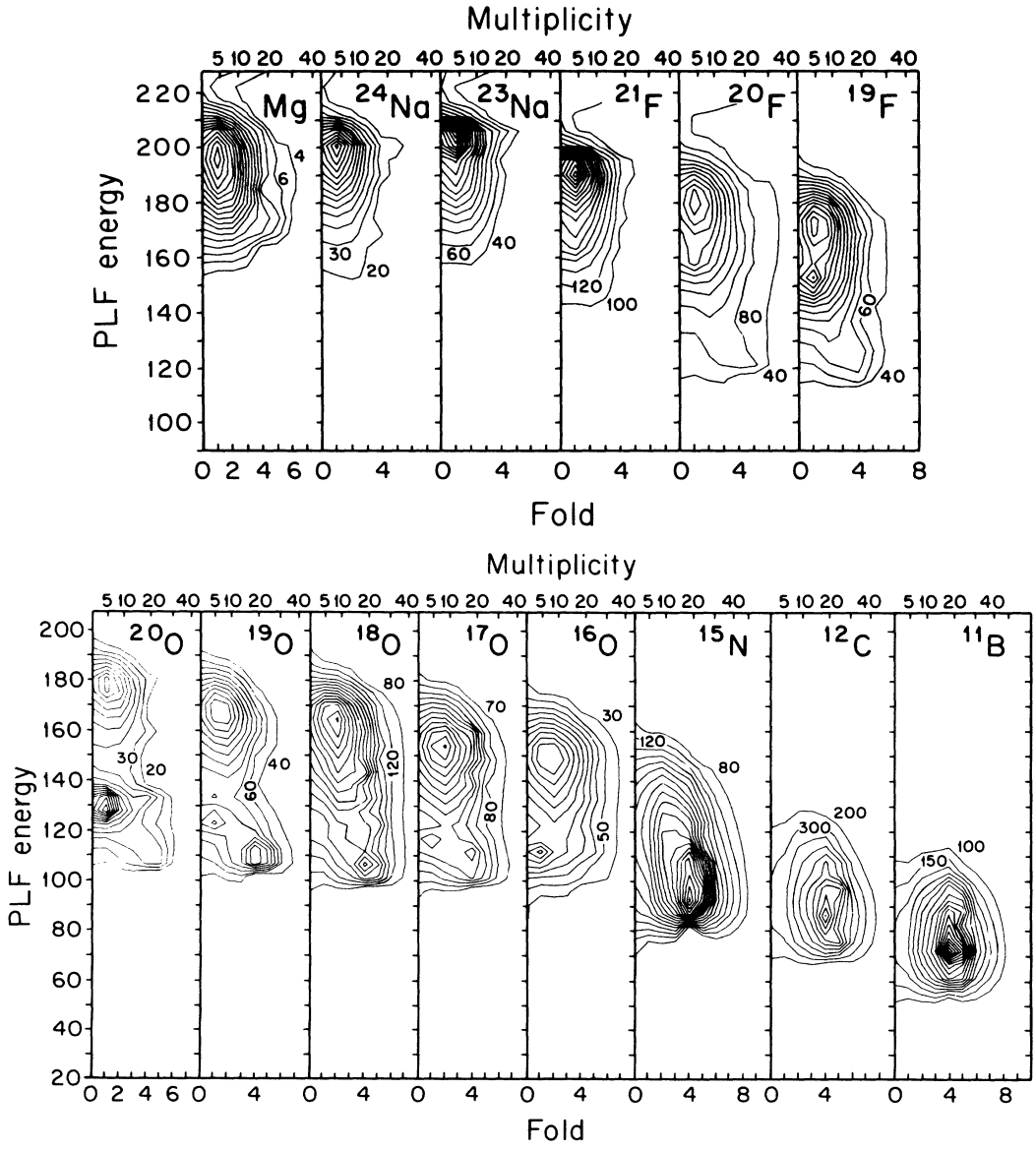

FIG. 3. PLF kinetic energy (E_{PLF}) vs fold plots for various PLF's, with an approximate multiplicity scale. This figure clearly shows the transition from almost completely quasi-elastic reactions for heavier PLF's to mainly DIC's for lighter PLF's. It also shows the greater γ-ray multiplicity induced by DIC's. The low-fold, low-energy peak in ^{19}F and some of the oxygen isotopes is associated with the strong elastic channel as noted in the caption in Fig. 2.

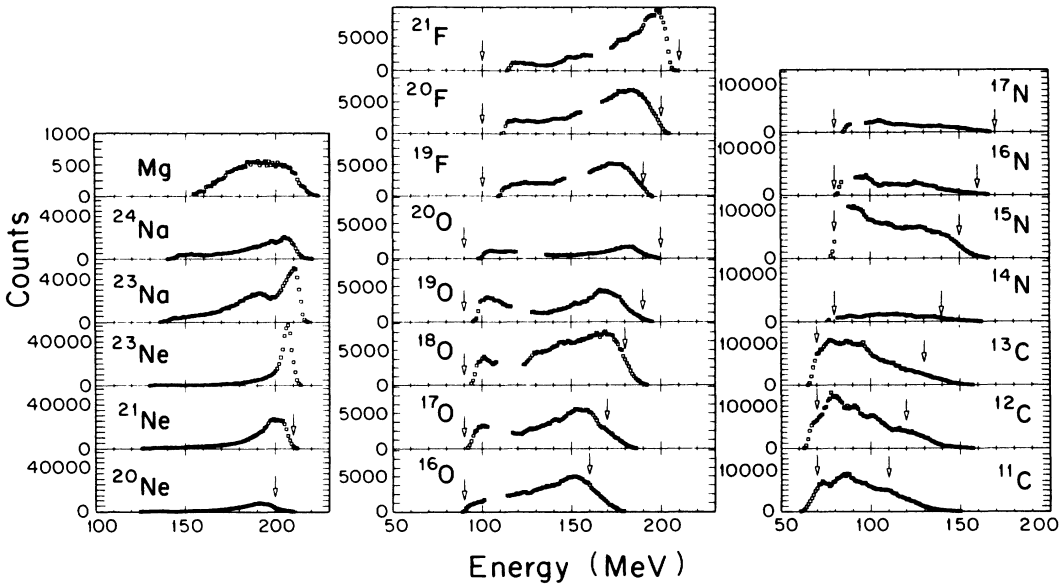

FIG. 4. E_{PLF} spectra for various PLF isotopes. The gaps in some of the plots occur where the spectrum is distorted by the elastic channel as noted in the caption to Fig. 2. Note the abrupt disappearance of the quasi-elastic peak between oxygen and nitrogen. The arrows at low and high PLF energies represent the Coulomb repulsion of the fragments and PLF kinetic energy at the beam velocity, respectively.

are tabulated in columns 2 and 3 of Tables II and III for QE and DIC, respectively. Column 4 lists the excitation energy $[E_x = E_x(\mathrm{TLF}) + E_x(\mathrm{PLF})]$ [see Eq. (9)] of the final system before any particle or γ-ray emission has taken place.

B. γ-ray multiplicity and angular momentum transfer

From the measured multiplicities, it is possible to estimate the fraction of the initial orbital angular momentum that is transformed into the spin angular momentum of the final fragments (TLF and PLF). The first stage in the decay of the highly excited states of the TLF's and PLF's consists of the evaporation of nucleons and α particles, until the fragments reach a state that is stable against particle emission. The average amount of angular momentum carried away by nucleon evaporation can be written as

$$\Delta I_n = \langle N_n \rangle \langle l_n \rangle \ , \tag{1}$$

where $\langle N_n \rangle$ and $\langle l_n \rangle$ designate the average number of nucleons emitted and the average amount of angular momentum carried away per nucleon. Statistical calculations using the code JULIAN-PACE (Ref. 13) as well as a considerable body of experimental data[14] indicate that $\langle l_n \rangle \simeq 0.7$. The average number of nucleons emitted can be estimated from the excitation energy E_x of the TLF according to

TABLE II. Columns 1 and 2 list the experimentally determined values of the PLF energy and the multiplicity of the quasi-elastic maxima. Columns 3 and 4 give the experimental and theoretical values for the excitation energy of the PLF immediately after the collision. For the meaning of the last four columns we refer to the text.

PLF	T_{QE} (MeV)	$M_{\mathrm{QE}}\gamma$	E_x (MeV)	$E_{x,\mathrm{th}}$ (MeV)	$\Delta I\gamma$	ΔI_n	I_i,exp	$I_{i,\mathrm{th}}$
^{24}Na	200	5.6	12		5	0	5	
^{23}Na	205	5.4	7		5	0	5	
^{21}F	190	5.4	13	14	5	0	5	4.5
^{20}F	180	5.6	22	20	5	1	6	9.0
^{19}F	172	5.7	30	26	5	1	6	13.5
^{20}O	177	6.0	28	28	6	1	7	9.0
^{19}O	166	7.3	32	34	9	2	11	13.5
^{18}O	168	9.3	34	40	13	2	15	18.0
^{17}O	154	10.3	46	45	15	3	18	22.5
^{16}O	144	8.9	58	51	12	3	15	27.0

TABLE III. Columns 1, 2, and 3 list the kinetic energy, multiplicity, and the excitation energy corresponding to the DIC maxima of Fig. 3. Columns 4 and 5 give the angular momenta carried away by evaporated nucleons and γ rays, respectively. Column 5 lists the experimentally derived angular momentum of the (TLF + PLF) system immediately after collision. Columns 7 and 8 list the angular momenta of the PLF and TLF as predicted by a friction model in the rolling limit (see text). Column 9 contains the sum $I_{\text{roll}}=I_{\text{PLF}}+I_{\text{TLF}}$ and should be compared with $I_{i,\text{exp}}$ in column 7. The last three columns list the analog quantities in the sticking limit.

	T_{DIC}		E_x				Rolling			Sticking		
PLF	(MeV)	$M_{\text{DIC}}\gamma$	(MeV)	ΔI_n	ΔI_γ	$I_{i,\text{exp}}$	I_{PLF}	I_{TLF}	I_{roll}	I_{PLF}	I_{TLF}	I_{stick}
^{20}F	130	15	71	4	23	27	11	23	34	2	75	77
^{19}F	127	14	75	5	25	30	11	23	34	3	77	79
^{20}O	113	17	86	5	28	33	11	23	34	2	75	77
^{19}O	109	17	88	6	28	34	11	23	34	2	77	79
^{18}O	105	15	96	6	24	30	11	24	35	2	80	82
^{17}O	111	14	88	6	23	29	11	24	35	2	79	81
^{15}N	91	18	103	7	32	39	10	24	35	1	85	86
^{12}C	85	19	105	7	32	39	10	25	35	1	91	92
^{11}B	73	20	106	7	33	40	10	25	35	1	93	94

$$\langle N_n\rangle=\frac{E_x-B_n-\langle K_n\rangle}{B_n+\langle K_n\rangle}\cong\frac{E_x-10\text{ MeV}}{10\text{ MeV}}\ , \tag{2}$$

where B_n is the binding energy per nucleon and $\langle K_n\rangle$ is the average kinetic energy of an evaporated nucleon. For the present analysis we obtained $\langle K_n\rangle=2$ MeV from PACE calculations and we assumed $B_n=8$ MeV.

Once the two fragments are stable against particle emission, the remaining angular momentum is carried away by γ emission. Most of the decays proceed via stretched $E2$ transitions (corresponding to a spin change $\Delta I=2$), while a small number N_s proceed by dipole transitions which, according to our statistical calculations, correspond to an average spin change of ΔI close to 0.5. Thus, we have $\Delta I_\gamma\cong 2(M-N_s)+N_s/2$, where M is the total γ multiplicity. In the present analysis we assumed $N_s=4.0$. The total amount of orbital angular momentum transformed into intrinsic angular momentum I_i is

$$I_i=\Delta I_n+\Delta I_\gamma\ . \tag{3}$$

The values for ΔI_n, ΔI_γ, and I_i corresponding to the quasi-elastic and deep inelastic maxima are listed in Tables II and III. In the following two sections we compare our experimental results with theoretical models for quasi-elastic and deep inelastic processes.

C. Quasi-elastic processes

In the simplest picture of a quasi-elastic transfer (QE) reaction, the velocity of the PLF equals that of the projectile. The corresponding PLF energies, indicated by arrows in Fig. 4, are systematically higher than the energies E_{QE} of the experimentally observed quasi-elastic maxima. The systematic trend of E_{QE} as a function of the PLF mass is, however, well reproduced.

A better understanding can be obtained if one invokes trajectory matching conditions. In the following analysis, the most probable experimental PLF velocities are extracted from the most probable PLF energies and compared with the predictions of a model by Siemens *et al.*[15] According to this model, the projectiles are slowed by Coulomb repulsion as they approach the target. At the top of the barrier, n nucleons are transferred from the projectile to the target, while m nucleons are picked up by the projectile from the target. The model furthermore assumes that these nucleons had, before the exchange, an average velocity equal to that of their parent nucleus (projectile or target). After the transfer, the PLF is accelerated by the Coulomb field in the exit channel. The relative velocity v_{Aa} between projectile and target just before the nucleon exchange is related to the relative velocity v_{Bb} between PLF and TLF just after the exchange according to

$$v_{Bb}=v_{Aa}\left[1-\frac{n}{B}-\frac{m}{b}\right]\ , \tag{4}$$

where a, A, b, and B are the mass numbers of the projectile, target, PLF, and TLF, respectively.

Energy conservation considerations allow one to provide the equations

$$\tfrac{1}{2}\mu_{Aa}v_{Aa}^2=T_i-U_i-e_i\ , \tag{5}$$

$$\tfrac{1}{2}\mu_{Bb}v_{Bb}^2=T_f-U_f+e_f\ , \tag{6}$$

where μ_{ij} is the reduced mass of the i,j system and T_i and T_f are the center-of-mass kinetic energies in the entrance and exit channels. U_i and U_f designate the barrier energies and are given by the sum of the Coulomb and nuclear potentials and can be written as follows:

$$\begin{aligned}U_i&=U_0+\frac{Z_AZ_ae^2}{r_0(A^{1/3}+a^{1/3})}\ ,\\ U_f&=U_0+\frac{Z_BZ_be^2}{r_0(B^{1/3}+b^{1/3})}\ .\end{aligned} \tag{7}$$

In our analysis, we use for the nuclear potential U_0 and the radius parameter r_0 the values of Siemens *et al.*: $U_0=-28$ MeV and $r_0=1.2$ fm. The quantities e_i and e_f represent the excitation energy imparted to the collision partners before and after particle transfer. It should be

noted that e_i and e_f constitute only a small part of the excitation energy of the final system. In Siemens *et al.*[15] these quantities are treated as adjustable parameters, typical values being $e_i = e_f = 3$ MeV. In our case, they are small enough to be neglected. In Fig. 5 a comparison is made between values of v_{Bb} derived from Eqs. (4) and (5) and experimental values derived from Eq. (6) using measured values of the PLF energy. The most probable PLF energies for fluorine and oxygen isotopes correspond to the quasi-elastic maxima in Fig. 3 (see also Table II). For the nitrogen isotopes, the quasi-elastic peak is not well defined in the total spectrum. Quasi-elastic peaks were, however, observable in spectra gated on low fold ($K < 2$), and these were used to find the most probable energies. The results of this analysis indicate that transfers with $A_{\text{PLF}} < A_{\text{projectile}}$ correspond to pure stripping reactions ($n \neq 0$, $m = 0$). Figure 5 also shows the most probable velocity for ^{23,24}Na and shows good agreement with a pure pickup hypothesis. Thus, all observed QE channels correspond to pure stripping or pure pickup reactions.

The model can be extended to make predictions concerning the transformation of orbital angular momentum into intrinsic angular momentum and the transformation of kinetic energy into excitation energy. To estimate the amount of angular momentum transferred to the target in a stripping reaction we assume, as before, that the transformed nucleons are left on the target surface with velocity v, inducing the rotation of the TLF. Using this assumption, the angular momentum transfer to the target is

$$I_{i,\text{th}} = nmvR_{\text{TLF}} = 4.5n\hbar \ , \tag{8}$$

where n is as before the number of nucleons transferred from the projectile to the target, m is the nucleon mass, v is the speed of the projectile, and $R_{\text{TLF}} = 1.2A_{\text{TLF}}^{1/3}$ is the radius of the TLF. The values for $I_{i,\text{th}}$ are listed in the last column of Table II. Comparison with the experimental values shows that this simple model accounts for the gross features of the angular momentum transfer as a function of the mass transfer.

It is also possible to determine the excitation energy E_x of the TLF. The experimental value of E_x corresponding to a given kinetic energy T_f of the PLF can be obtained from the Q-value equation

$$T_f = T_i + Q_{\text{g.s.}} - E_x \ , \tag{9}$$

in which T_i is the kinetic energy in the entrance channel. A theoretical value for the excitation energy can be derived by calculating T_f from Eq. (6) using theoretical values for v_{Bb}. These quantities are compared in Table II, column 5, with values of E_x derived using the measured values of T_f. As can be seen, the theoretical and experimental values are in good agreement.

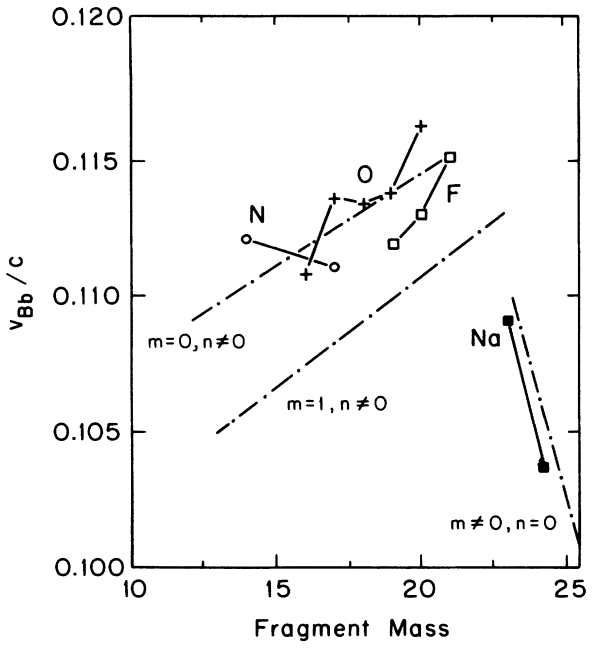

FIG. 5. The experimental QE PLF velocities for F, O, N, and Na isotopes are shown as a function of the fragment mass. The experimental points associated with the isotopes of a given element are connected by solid lines. The dot-dashed lines represent the velocities expected from a simple trajectory matching model (see text) for a pure stripping process ($m = 0$, $n \neq 0$), a pure pickup process ($m \neq 0$, $n = 0$) and a "mixed" process ($m = 1$, $n \neq 0$) as indicated.

D. Deep inelastic collisions

There exists a considerable literature dealing with deep inelastic processes.[16–18] Here we are primarily interested in the transformation of orbital angular momentum into intrinsic angular momentum and the sharing of the latter between the TLF and the PLF. The models that deal with these questions can be divided into two major classes, i.e., microscopic and macroscopic models. In microscopic models, the exchange of angular momentum and excitation energy is viewed in terms of the diffusion of nucleons between the two fragments during the time of significant overlap.

The present analysis is based on a classical, macroscopic model and follows the general treatment given by Tsang[16] to deep inelastic collisions. According to this model, the microscopic degrees of freedom are replaced by four collective parameters, namely, the distance between the two colliding nuclei, the angle of rotation of the line joining their centers, θ_{12}, and the angle of self-rotation of the two nuclei, θ_{PLF} and θ_{TLF}. The shape of both nuclei are taken as spherical. The inclusion of θ_{PLF} and θ_{TLF}, however, allows the treatment of the angular momenta I_{PLF} and I_{TLF} in the model.

Briefly, the model describes the collision using equations of motion obtained from the Lagrange-Rayleigh method, in which a first-order velocity-dependent frictional force is introduced. During the initial stages of the collision, the sliding friction results in the transfer of initial orbital angular momentum (L_0) into spin angular momentum (I_{PLF} and I_{TLF}). As the system evolves in time the two nuclei start to roll against each other, and the so-called "rolling" friction begins to dissipate energy. This can eventually bring the nuclei to the "sticking' lim-

it where they move together as a whole. Thus, the amount of orbital angular momentum transferred to the internal degrees of freedom is dictated by how far the system has evolved before the separation of the PLF and TLF.

For the limiting cases it is possible to give closed form expressions for the fraction of the initial orbital angular momentum that is transformed into the spin angular momenta of the PLF and TLF. For the rolling limit,

$$\frac{I_{\mathrm{PLF}}}{L_0}=\frac{2}{7}\frac{R_{\mathrm{PLF}}}{R_{12}} \quad \text{and} \quad \frac{I_{\mathrm{TLF}}}{L_0}=\frac{2}{7}\frac{R_{\mathrm{TLF}}}{R_{12}}\ , \tag{10}$$

for the sticking limit,

$$\frac{I_{\mathrm{PLF}}}{L_0}=\frac{\mathcal{J}_{\mathrm{PLF}}}{\mathcal{J}_{12}+\mathcal{J}_{\mathrm{PLF}}+\mathcal{J}_{\mathrm{TLF}}} \tag{11a}$$

and

$$\frac{I_{\mathrm{TLF}}}{L_0}=\frac{\mathcal{J}_{\mathrm{TLF}}}{\mathcal{J}_{12}+\mathcal{J}_{\mathrm{PLF}}+\mathcal{J}_{\mathrm{TLF}}}\ , \tag{11b}$$

where $\mathcal{J}_{\mathrm{PLF}}$ and $\mathcal{J}_{\mathrm{TLF}}$ are the rigid moments of inertia of the fragments, $\mathcal{J}i=\frac{2}{5}M_iR_i^2$, and $\mathcal{J}_{12}=\mu R_{12}^2$. The radii are given by $R_i=1.2A_i^{1/3}$, and $R_{12}=R_{\mathrm{PLF}}+R_{\mathrm{TLF}}$.

The values obtained using the above expressions are shown in columns 7, 8, 10, and 11 of Table III. Columns 9 and 12 show the total amount of orbital angular momentum that is transformed into intrinsic angular momentum. These values can be compared with the experimentally derived angular momentum $I_{i,\mathrm{exp}}$ of the system, which is given in column 6. In the sticking limit, one expects the amount of L transfer to increase with increasing mass transfer. In the rolling limit, the total amount of transferred angular momentum is constant for all TLF's. The latter picture better describes the experimental results obtained for DIC in this work, which shows an angular momentum transfer of about $33\hbar$ for all the investigated TLF's. This can be better seen in Fig. 6 where the average I_{TLF} for several PLF's is plotted together with the values from both the sticking and the rolling limits.

The selection of the rolling limit is favored in our experiment because all the PLF detectors were placed near the grazing angle for the reaction. A gradual shift to the sticking limit can be expected as the detectors are moved to more backward angles, as described by LeFort and Ngô.[19]

E. Exclusive and inclusive cross sections: Spectroscopy and reaction mechanisms

Due to the ability to completely identify both the PLF and the associated TLF's, it was possible to obtain detailed information concerning the reaction mechanism. Figure 7 shows the γ spectra in coincidence with each PLF isotope with $Z\geq 6$. In each case, the spectrum is the sum of the spectra from all five HPGe detectors. The spectra were Doppler corrected on the basis of the reaction kinematics. The most prominent lines are labeled according to the TLF isotope of origin.

Tables IV and V summarize the exclusive relative cross

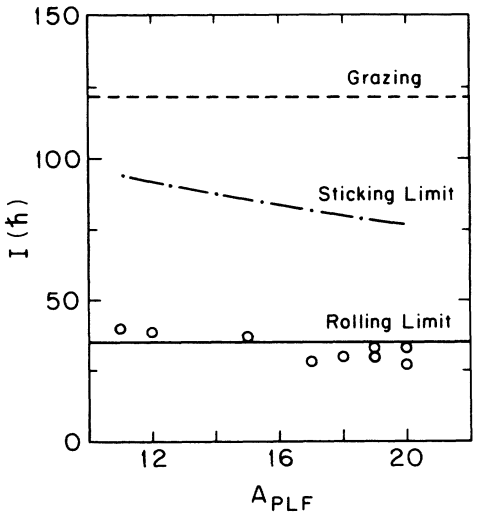

FIG. 6. Average amount of orbital angular momentum that is transferred into intrinsic angular momentum in deep inelastic collisions, as a function of PLF mass. The circles represent the experimentally derived values. The theoretical values for the rolling and sticking limit are also shown. The dashed line indicates the grazing angular momentum in the present experiment.

sections for the production of TLF's in coincidence with ^{16,17,18,19,20}O and ^{11,12,13}C. The yields are given in percent of the elastic cross section. These yields were derived from the lowest observable transitions and were corrected for the HPGe-detector efficiency, internal conversion, and branching ratios. For the even-even isotopes, the $6^+\rightarrow 4^+$ transition was used. In cases where this transition was a member of a poorly resolved doublet, the $8^+\rightarrow 6^+$ transition was employed instead. Odd isotopes were identified on a case-by-case basis using transitions that provided the most unambiguous assignment.

Figure 7 shows that in all oxygen channels, the Yb and Er isotopes are populated. The ^{11,12,13}C channels are in coincidence with Hf and Yb nuclei. The population of the Yb (Hf) isotopes in coincidence with oxygen (carbon) PLF's is best understood in terms of a binary transfer reaction followed by the evaporation of neutrons. Below we present calculations which show that the population pattern of the Yb isotopes associated with ^{18}O PLF's can be well understood in terms of such a picture.

The last row in Tables IV and V lists the average number of neutrons emitted in the binary channels and illustrates that this number increases with the number of particles transferred. This is as expected, since the inelasticity of the reaction, and hence the excitation energy of the final system, increases with the number of particles transferred. The increase in average excitation energy with the number of particles transferred is also evident from the PLF energy spectra in Fig. 4 and is consistent with results by Wilczynski *et al.*[5] for the system ^{14}N+^{159}Tb. Row 8 in Table IV lists for each oxygen PLF the total cross section for populating Yb isotopes, while row 14 gives the total cross section for the formation of Er isotopes. In both cases the cross section reaches a maximum for ^{18}O which corresponds to the α

transfer and α breakup channel, respectively. It is well known from shell-model calculations that the ^{22}Ne wave function contains a significant α-cluster component.[20] This seems to be the most likely explanation for the dominance of these channels.

The observation in Table IV (V) and Fig. 7 of transitions in the Er (Yb) isotopes in coincidence with ^{16,17,18,19,20}O (^{11,12,13}C) must be associated with the emission of unobserved charged fragments. Statistical calculations using the code JULIAN-PACE indicates that less than 2% of these cross sections can be attributed to charged particle evaporation from the TLF's and therefore show that these fragments must be associated with projectile breakup.

A question of considerable interest concerns the time scale for projectile breakup. Two limiting regimes are typically considered and referred to as a direct breakup and sequential breakup. Direct breakup refers to the breakup of the projectile while it is still interacting with the target nucleus. Utsunomiya *et al.*[9] have argued that this mechanism is associated with very little excitation of the TLF and hence small γ-ray multiplicity, and it is then referred to as cold breakup. Later in this section we present evidence that cold breakup is not a significant component in the present experiment. Sequential decay refers to a two-step process in which the projectile is given a significant amount of excitation energy during its interaction with the target and decays later after it is well outside the range of interaction.

Experiments by Homeyer *et al.*[21] show that 15-MeV/nucleon ^{20}Ne ions impinging on ^{197}Au dissociate via sequential decay into ^{16}O+α. Similar results were obtained in a recent experiment by Shimoda *et al.*,[22] who investigated the system ^{20}Ne+^{40}Ca at several energies between 4.6 to 10.7 MeV/nucleon.

Our experiment does not yield direct information about the time scale of the breakup mode, but in view of the results of Refs. 21 and 22 it must be assumed that sequential breakup is the dominant mode. The second- and third-to-last rows in Tables IV and V show the division of the cross section between binary (transfer) and projectile breakup processes. For the oxygen PLF's, we find that binary processes are dominant, accounting for ~80% to 90% of the total exclusive yield. This is con-

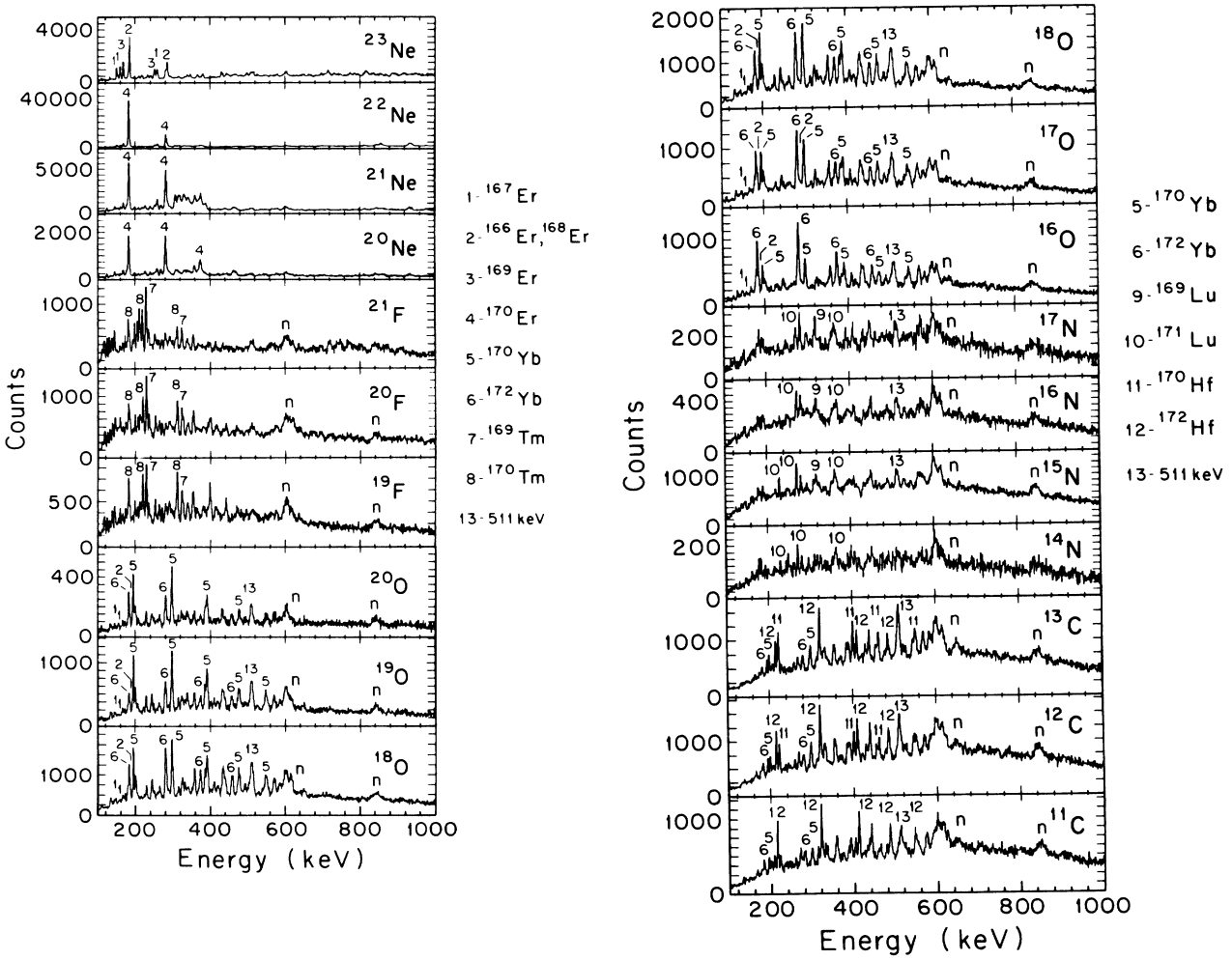

FIG. 7. γ-ray spectra created by gating on various PLF isotopes. γ-ray lines associated with selected TLF channels are marked. Peaks labeled by "n" are events originating from neutron scattering in the HPGe crystal.

TABLE IV. Exclusive relative cross sections in percent of the elastic cross section for the oxygen PLF's. The third- and second-to-last rows give the division of the cross section between binary and breakup processes. The last row lists the average number of neutrons emitted in binary reactions.

TLF \ PLF	^{16}O	^{17}O	^{18}O	^{19}O	^{20}O
^{172}Yb	0.17(1)	0.11(1)	0.21(1)	0.056(8)	0.096(4)
^{171}Yb	0.094(9)	0.16(1)	0.20(2)	0.13(1)	0.049(4)
^{170}Yb	0.075(6)	0.17(1)	0.22(1)	0.17(1)	0.066(3)
^{169}Yb	0.067(5)	0.078(8)	0.14(1)	0.077(6)	0.032(3)
^{168}Yb	0.027(5)	0.073(6)	0.10(1)	0.030(5)	0.11(2)
^{167}Yb	0.020(2)	0.033(3)	0.040(4)	0.030(7)	0.017(2)
^{166}Yb		0.026(5)	0.032(5)	0.038(6)	0.017(2)
Total Yb	0.453(16)	0.642(21)	0.95(29)	0.537(20)	0.228(8)
^{168}Er	0.033(5)	0.036(5)	0.047(6)		0.008(1)
^{167}Er	0.050(4)	0.015(2)	0.050(4)	0.011(1)	0.007(1)
^{166}Er	0.023(4)	0.032(5)	0.050(7)	0.030(5)	0.011(1)
^{165}Er	0.015(2)	0.047(4)	0.020(2)	0.018(3)	0.008(1)
^{164}Er	0.012(3)	0.021(4)	0.020(4)	0.013(3)	0.005(1)
Total Er	0.133(8)	0.151(9)	0.187(11)	0.072(7)	0.039(2)
Binary (Yb)	79%	79%	82%	86%	88%
Sequential breakup (Er)	21%	21%	18%	14%	12%
$\langle n \rangle$	5.5	5.1	4.0	3.2	2.2

TABLE V. Exclusive relative cross sections in percent of the elastic cross sections for the carbon PLF's. The third- and second-to-last rows give the division of the cross section between binary (i.e., transfer) and breakup processes. The last row gives the average number of neutrons emitted in binary reactions.

TLF \ PLF	^{11}C	^{12}C	^{13}C
^{174}Hf	0.040(3)	0.029(3)	0.032(3)
^{173}Hf	0.076(6)	0.114(9)	0.074(7)
^{172}Hf	0.100(4)	0.111(4)	0.086(4)
^{171}Hf	0.114(9)	0.131(10)	0.101(9)
^{170}Hf	0.032(4)	0.078(4)	0.100(4)
^{169}Hf	0.033(3)	0.012(1)	0.063(7)
^{168}Hf	0.020(2)	0.013(2)	0.009(2)
Hf total	0.415(13)	0.488(15)	0.464(15)
^{174}Yb	0.018(2)	0.016(3)	0.015(3)
^{173}Yb	$<$0.025	$<$0.025	$<$0.024
^{172}Yb	0.034(3)	0.037(3)	0.029(3)
^{171}Yb	0.035(3)	0.039(3)	0.034(3)
^{170}Yb	0.040(3)	0.051(3)	0.045(3)
^{169}Yb	0.036(3)	0.051(3)	0.055(4)
^{168}Yb	0.028(3)	0.054(6)	0.058(3)
^{166}Yb	0.025(3)	0.031(2)	0.034(3)
^{166}Yb	0.018(2)	0.035(5)	0.036(3)
^{165}Yb		$<$0.20	$<$0.025
^{164}Yb		0.007(2)	$<$0.010
Yb Total	0.26(1)	0.37(1)	0.37(1)
Binary (Hf)	62%	57%	56%
Sequential breakup (Yb)	38%	43%	44%
$\langle n \rangle$	9.5	8.4	7.8

sistent with qualitative results by Dünweber,[23] on the system ^{20}Ne+^{168}Er at a bombarding energy of 13.5 MeV/nucleon. For the carbon PLF's, we find that 56% to 62% of the yield is associated with binary reactions. This is in sharp contrast to the work of Ref. 23 which identified only Yb isotopes (corresponding to PLF breakup) but shows no evidence for populating Hf isotopes.

The conditions in the experiment of Dünnweber and our own experiment essentially differ in three respects, namely, (a) the initial system: ^{20}Ne+^{168}Er vs ^{22}Ne+^{170}Er; (b) bombarding energy: 13.5 MeV/nucleon vs 10 MeV/nucleon; and (c) the scattering angle: 25° vs 30°. The two experiments also differed in some technological aspects. Our use of five Compton-suppressed Ge detectors resulted in superior peak-to-total ratios for the γ-ray spectra with considerably better sensitivity to weak transitions, and our use of surface barrier telescopes gave good isotope resolution. It is not clear at this point whether the observed differences are due to any of these factors.

A much-debated question concerns the ratios of exclusive to inclusive cross sections. Our results are given in row 4 of Table VI and show that, on average, the exclusive cross section is only about half that of the inclusive cross section. Thus, roughly half of the inclusive cross section is not associated with identified discrete γ rays. Table VI also summarizes the results of several other experiments. The work of Wilzcynski *et al.*,[5] and Utsunomiya *et al.*,[9] was based on PLF-γ-coincidence experiments similar to our own. In the first three rows of Table VI, our ratio of binary to inclusive cross section for the carbon and oxygen isotopes is compared with the fraction of binary reactions, determined by Wald *et al.*,[24]

TABLE VI. Row 1 lists the ratio of binary to inclusive cross sections measured in the present experiment. Row 2 lists the same ratio corrected for missing γ rays (see text). Row 3 gives the results of Ref. 24. Columns 4 and 10 list the average overall carbon and oxygen isotopes, respectively. Column 11 gives the average overall PLF's. Rows 4, 5, and 6 list the ratios of exclusive to inclusive cross sections obtained in the present experiment and similar experiments by Refs. 9 and 5.

	^{11}C	^{12}C	^{13}C	⟨C⟩	^{16}O	^{17}O	^{18}O	^{19}O	^{20}O	⟨O⟩	Average overall PLF's	System	Energy	Reference
Binary/inclusive Measured	27%	26%	28%	27%	31%	39%	36%	39%	37%	36.5%		^{22}Ne+^{170}Er	10 MeV/u	Present work
Binary/inclusive Corrected	61%	56%	56%	57%	75%	80%	80%	87%	73%	79%				Present work
Binary/inclusive				57%						78%		^{20}Ne+^{197}Au	10 MeV/u	Ref. 24
Exclusive/inclusive	44%	46%	50%	47%	42%	49%	45%	45%	51%	46%	47%	^{22}Ne+^{170}Er	10 MeV/u	Present work
Exclusive/inclusive											10% 10%	^{14}N+^{164}Dy ^{14}N+^{165}Ho	20 MeV/u	Ref. 9
Exclusive/inclusive											20%	^{14}N+^{159}Tb	10 MeV/u	Ref. 5

for the system ^{20}Ne+^{197}Au at 10 MeV/nucleon. In that experiment, the fraction of the charge binary cross sections and the charge breakup cross section (i.e., more than two charged fragments in the final state) were determined using a 4π charged particle detector array.

It should be noted that the exclusive-to-inclusive ratios presented here are considerably larger than those of Refs. 5 and 9. This may, in part, be due to differences in the systems considered and, in the case of Ref. 9, to the difference in bombarding energy. The difference between our results and those of Ref. 5 by a factor of 2 to 3 calls for some discussion. It should be noted that exclusive cross sections determined by particle-γ coincidences represent lower limits, since some γ rays associated with sufficiently weak channels will always be missed. Just how much cross section is missed will depend on the technology used and on the amount of statistics accumulated. Thus at least part, and possibly all, of the difference may be attributable to the better peak-to-total ratios that were obtained in the present experiment by using Compton-suppressed Ge detectors.

The ratios of binary to inclusive cross sections obtained in the present experiment (line 1 in Table VI) are still considerably lower than the results obtained by Wald *et al.*[24] for the system ^{20}Ne+^{197}Au (line 3 in Table VI). Part, and possibly all, of this difference may again be attributed to missing γ rays associated with weak channels. If one assumes that all of the missing exclusive cross section is due to missing γ rays, one can construct from our data a "corrected" binary to inclusive cross section by dividing the measured binary-inclusive ratios (row 1, Table VI) by the measured exclusive-inclusive ratios (row 4). The results of this procedure is shown in row 2 of Table VI and can be compared with the results of Wald *et al.*[24] in row 3. The excellent agreement between the two sets of data suggests that the projectile breakup mechanism depends on the projectile only and is independent of the target.

It has been suggested[9] that the difference between inclusive and exclusive cross sections may be due to "cold" breakup, in which the TLF is given very little or no excitation energy. This seems rather unlikely, since one would expect in such close encounters a considerable amount of inelastic excitation (including Coulomb excitation). Figures 8(a) and 8(b) show the fold-multiplicity distributions for ^{18}O corresponding to inclusive and exclusive events. Figure 8(c) shows the difference between the two (inclusive minus exclusive) which corresponds to the fold-multiplicity distribution of the "missing" cross section. The average multiplicity of the missing cross section is only slightly less than for the exclusive cross section (7.3 vs 9.4). This is inconsistent with the assumption that cold breakup is the dominant mode in the missing cross section. The multiplicity associated with the missing cross section is sufficiently high that the corresponding γ rays should manifest themselves in the high-resolution HPGe spectra. The fact that they cannot be

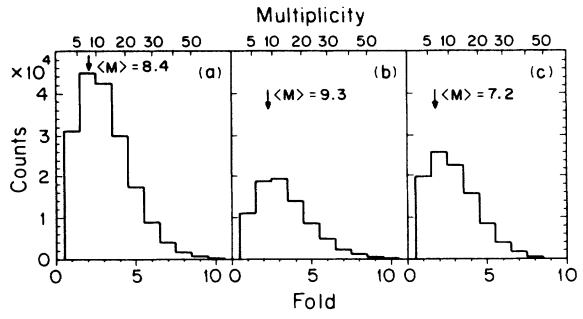

FIG. 8. Fold-multiplicity distributions for (a) inclusive data, (b) exclusive (PLF-γ) data. Panel (c) shows the difference of inclusive-exclusive data. The average fold values are indicated by the arrows.

associated with identifiable discrete lines seems to indicate that a significant fraction of the reaction yield is spread over many weak channels. One expects, in particular, that lines from many of the odd-odd and even-odd TLF's have been missed. Finally, it should be noted that side feeding into states below the 6^+ or 4^+ states could account for some of the "missing" cross section since the analysis was based primarily on the 4^+-2^+ and 6^+-4^+ transitions.

F. Projectile excitation

Using the kinematic information provided by the particle telescopes, it was possible to create γ-ray spectra Doppler shifted into the rest frame of the PLF's. Figure 9 shows three such spectra in coincidence with ^{17}N, ^{18}O, and ^{19}F. It is clear from these spectra that very often the PLF is also excited during the reaction process. For the ^{18}O PLF, the relative yield for this process can be calculated. In about 50% of the total events, the ^{18}O PLF is excited. The average excitation of ^{18}O PLF is of the order of 2 or 3 MeV, while the excitation of the system is typically an order of magnitude higher.

G. γ-PLF coincidence spectroscopy

PLF energy versus γ-ray energy coincidence matrices were constructed for several PLF isotopes. In each case, separate matrices were constructed for events with low fold ($0 < k < 3$) and high fold ($k \geq 4$). In addition, separate matrices were constructed for time-correlated and uncorrelated events (timing "foreground" and "background") for a total of four matrices per isotope.

By placing gates on discrete TLF γ-ray energies, it was possible to obtain PLF kinetic-energy spectra corresponding to particular subchannels. Figure 10 shows the PLF energy spectra for ^{18}O in coincidence with several Yb isotopes. In Fig. 11 we plot similar spectra for ^{12}C in coincidence with some Yb and Hf isotopes. For the purpose of comparison we plot in Fig. 12 the energy spectra of ^{12}C, ^{16}O, and ^{18}O, each gated on ^{168}Yb. In all of these spectra, gates were set on the 4^+-2^+, $6^{\pm}$-4^+, 8^+-6^+, and in some cases, 10^+-8^+ transitions of the TLF, with random background subtracted. The discrete spacing of the maxima on Figs. 10–12 suggests the possibility of selectively enhancing a specific TLF subchannel by gating on an appropriately chosen PLF energy interval. This worked quite well for the stronger Yb subchannels in coincidence with ^{18}O as shown in Fig. 13. In channels such as ^{12}C, there can be more than one strong subchannel at a given PLF energy, making this kind of separation less effective though still useful.

The observed TLF isotope selectivity as a function of the PLF energy can be understood as a process in which an initial compound system consisting of the target nucleus and the transferred cluster is formed, and subsequent light particle evaporation takes place (see, e.g., Ref. 9). In order to have a more quantitative description of this picture, a statistical model calculation, making use of the code JULIAN-PACE (Ref. 13), was performed for the ^{18}O exit channel.

For the calculation, the PLF energy spectrum was divided into 10-MeV-wide bins and the associated excitation energy determined. A sharing of excitation energy between PLF and TLF according to the ratio of their masses was assumed except for quasi-elastic energies, where it was assumed that the total excitation energy is deposited in the TLF. The first and second moments of the multiplicity distribution correspond to each PLF energy bin were derived from the data. This information was converted into angular momentum distributions using the procedure discussed in Sec. III B. The excitation energy and angular momentum distributions were used as input for the JULIAN-PACE calculation. From the output

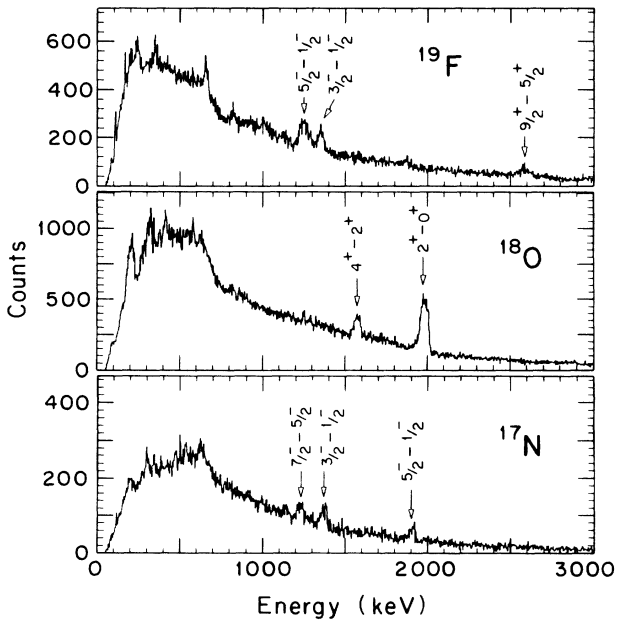

FIG. 9. γ-ray spectra with Doppler shifts for PLF velocity. The spectra were generated for events in coincidence with the PLF's indicated in the figures. Characteristic transitions for each PLF are indicated.

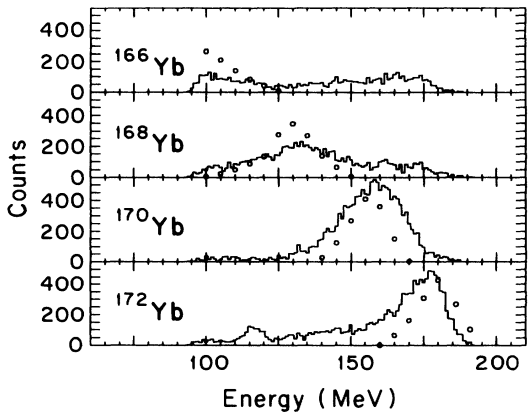

FIG. 10. ^{18}O energy spectra gated on γ-ray lines for various TLF's, along with results from statistical decay calculation (circles) as described in Sec. III G.

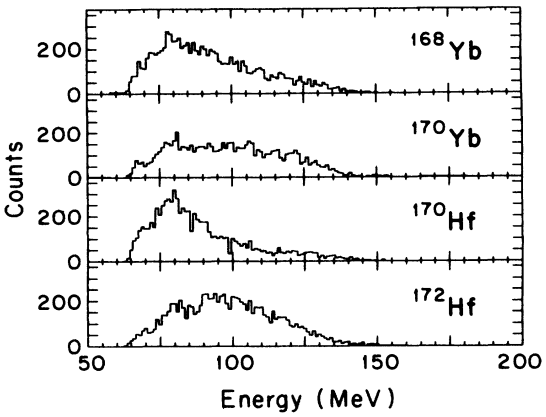

FIG. 11. ^{12}C energy spectra gated on the γ-ray lines of several TLF's.

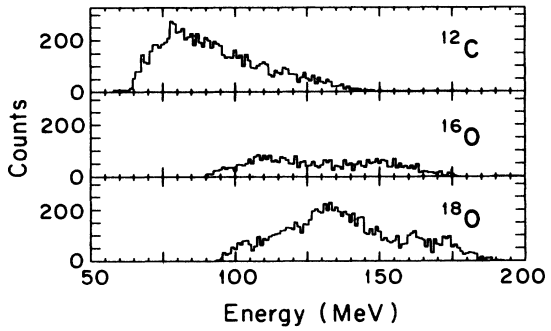

FIG. 12. E_{PLF} spectra for ^{12}C, ^{16}O, and ^{18}O gated on ^{168}Yb γ-ray lines.

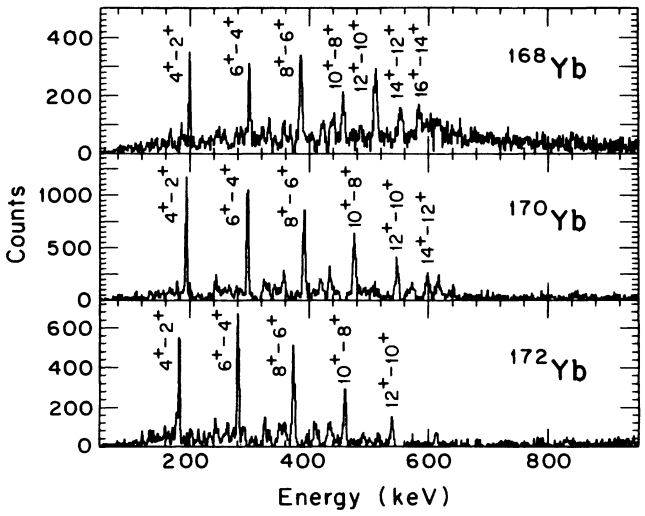

FIG. 13. TLF γ-ray spectra obtained by gating on different energies of the ^{18}O PLF. The energy ranges of the gates are 122 to 137 MeV (top), 144 to 163 MeV (middle), and 173 to 191 MeV (bottom).

of the latter, it is then possible to construct the TLF mass distribution as a function of PLF energy.

In Fig. 10 these results are shown as circles. The calculated peak positions and widths agree satisfactorily with the corresponding experimental spectra, except for ^{172}Yb. The preferential population of this isotope can probably be best understood in terms of preequilibrium emission of neutrons. The distributions for other isotopes in which the primary TLF is produced in more inelastic reactions are well described, indicating their statistical nature.

The calculation also shows a small amount of erbium populated via αxn evaporation channels. These channels account for about 25% of the total cross section. Calculations were also performed for other isotopes, and the agreement with the experimental results is satisfactory for channels arising from transfers of light clusters. In cases such as the ^{12}C exit channel, in which a total of 10 nucleons are transferred, the yields of some residual isotopes observed experimentally are not well reproduced by the calculations.

H. γ-γ coincidence spectroscopy

To investigate the possibility of using the reaction under study for spectroscopic purposes, γ-γ coincidence events were acquired. For this set of data, no coincidence with any PLF was required and, consequently, no restrictions with respect to the impact parameter or reaction channels were present.

Figure 14 shows the total γ-ray spectra for both γ-γ and PLF-γ coincidences. The spectra are quite similar except that the γ-ray lines associated with inelastic excitation of the target appear much more strongly in the PLF-γ spectrum. This can be attributed to the fact that the requirement of γ-γ coincidence favors events with high multiplicities. Peaks in the spectra indicated by "n" are due to inelastic scattering of neutrons in the detector crystal.

In the analysis, the strongest peaks in the PLF-γ data described above were also observed in the γ-γ data with

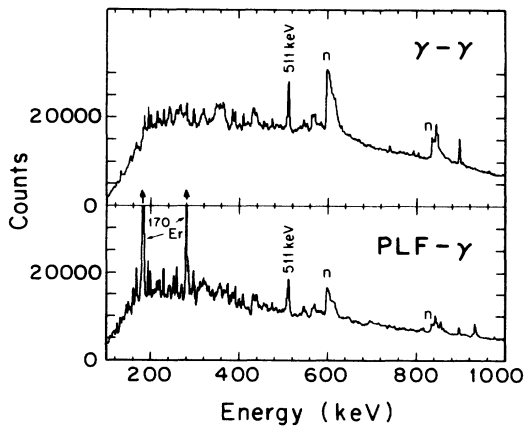

FIG. 14. Total γ-ray spectra for the γ-γ (top) and PLF-γ (bottom) data. The ^{170}Er Coulomb excitation peaks are off scale for the PLF-γ data.

similar strengths. The similarities of γ-ray intensities arise from the fact that, at these bombarding energies, most of the reaction cross section is due to deep inelastic and quasi-elastic reactions. Critical angular momentum considerations show that the fusion cross section is, at most, 30% of the total reaction cross section.[25]

The analysis of the γ-γ coincidence events was carried out in a way similar to that of PLF-γ events. After the gain equalization was applied to the five germanium detectors, the coincidence pairs were used to construct a coincidence matrix $E_{\gamma 1}$ vs $E_{\gamma 2}$. A matrix of uncorrelated events, based on timing information, was also constructed in order to substrate accidental coincidences.

Once the $E_{\gamma 1}$ vs $E_{\gamma 2}$ matrix was constructed, gates were set on known transitions and a "gated" γ-ray spectrum, corresponding to a given TLF isotope, was obtained. Besides the subtraction of time-uncorrelated events, a proximity background, defined by a gate on the γ-ray energy region near the TLF γ rays of interest, was also subtracted. This allows the subtraction of other uncorrelated events, such as Compton background, background due to events associated with inelastic neutron scattering, etc.

Typical γ-ray spectra for ^{170}Yb and ^{168}Yb are shown in Fig. 15. Despite the rather complex structure of the total γ-ray spectrum, shown in the top section of Fig. 14, it was possible to enhance the spectra of these isotopes through suitable gates. The same kind of analysis was applied to lines of other isotopes, and similar results were derived. The transitions shown here are mostly transitions in the yrast band and most of them have been previously identified in other reactions.[26,27] Limited statistics prevented us from drawing more conclusions about the spectroscopic properties of the levels populated in the reactions, but some comments on the results of the analysis can be made.

In the analysis of ^{170}Yb, a transition with $E_\gamma = 631$ keV was observed in coincidence with transitions in the Yrast band. This transition has been tentatively assigned by Walker *et al.*[26] as a 20^+ to 18^+ transition. Our data does not permit a confirmation of this assignment, but our data corroborates the previous assignments since the energy of the level and its intensity are in good agreement with the systematics of other transitions in this band. In addition, an 816-keV γ ray was found in coincidence with the $(4^+$-$2^+)$ transition of ^{168}Yb. A tentative assignment of a 3^+ level at 1103 keV has been made.

I. Population of high spin states

In order to compare the populations of high spin states in the $A \sim 170$ region via different reaction mechanisms, a comparison of transition intensities as a function of angular momentum was made. In Fig. 16 a plot of transition intensity as a function of the spin of the initial state is shown for four Yb isotopes in coincidence with ^{18}O. This figure shows how the excitation of angular momentum changes according to the reaction mechanism involved. For ^{172}Yb and ^{170}Yb, which are produced primarily by quasi-elastic reactions (see Fig. 10), the intensity drops off quite rapidly for transitions above the 8^+ state. As we move towards isotopes that are populated primarily through DIC, the intensities do not fall off as rapidly at higher spins. Similar distributions can also be seen in Fig. 17, in which the same plots have been made for TLF's in coincidence with ^{12}C. Here are shown distributions for both Yb and Hf isotopes.

It is interesting to compare the relative γ-ray intensities obtained in PLF-γ coincidences with those obtained from γ-γ coincidences. This comparison is shown in Fig. 18, where the intensities are normalized at $I = 4\hbar$. In general, the observed intensities in the γ-γ data drop more rapidly than the intensities for particle-γ events. This is presumably due to the lack of selection in the impact parameter for γ-γ events. In the case of particle-γ events, mostly peripheral collisions and scattering at negative angles due to DIC are selected, so that a narrower and higher angular momentum window is being probed. Also included in this figure is the γ-ray intensity distribution for inelastic excitation of the target. This intensity distribution drops off sharply at higher spins, indicating a rather small angular momentum transfer in the present

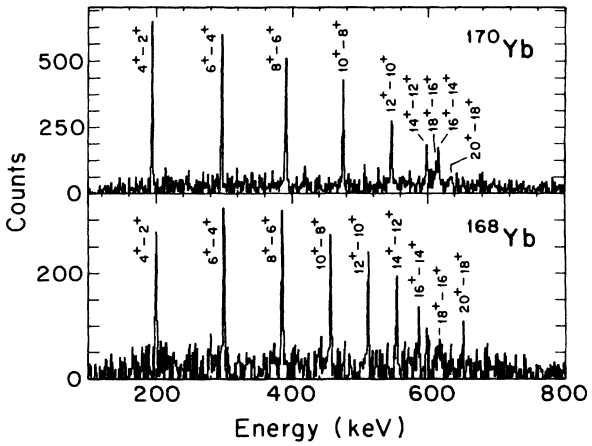

FIG. 15. γ-ray spectra for ^{168}Yb and ^{170}Yb, obtained from the γ-γ data by summing spectra gated on several transitions.

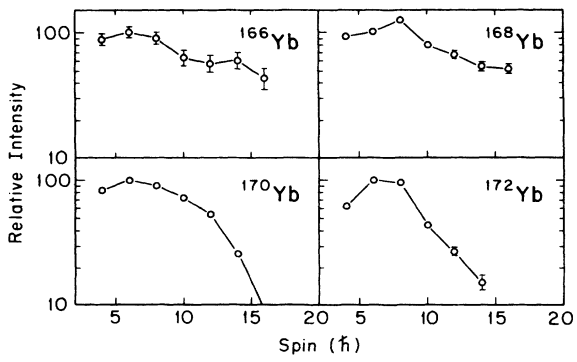

FIG. 16. Relative transition intensities as a function of initial state spin for the yrast lines of four Yb isotopes gated on ^{18}O. The intensity drops off more rapidly for the heavier isotopes, indicating a lower angular momentum. The plots are normalized to the 4^+-2^+ transition.

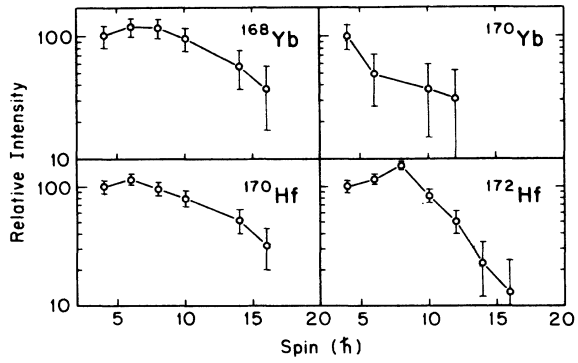

FIG. 17. Relative transition intensities as a function of spin for four TLF's in coincidence with ^{12}C.

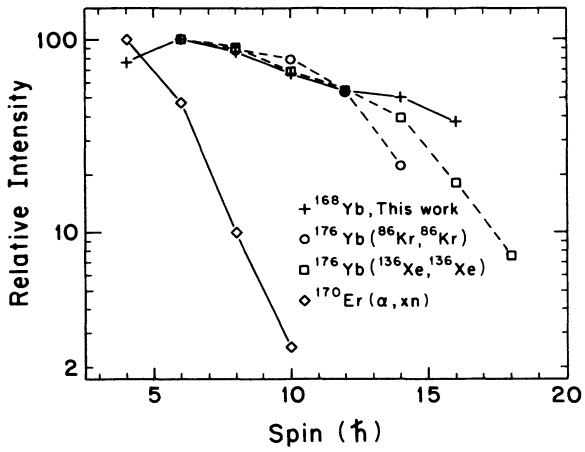

FIG. 19. Relative transition intensities for ^{168}Yb compared to similar intensities from a heavy projectile Coulomb excitation (Ref. 28) experiment and an (α,xn) (Ref. 29) reaction.

reaction. This behavior is expected since forward scattered projectiles are not expected to cause multiple inelastic excitation.

In order to compare how effectively DIC's can populate high spin states relative to previously studied reactions, we show in Fig. 19 our intensity distribution for ^{168}Yb together with Coulomb excitation reactions for $^{174,176}Yb$,[28] induced by ^{86}Kr and ^{136}Xe. We also include in this figure an intensity plot for $^{170}Er(\alpha,2n)$ (Ref. 29) at 19 MeV. It is clear from the figure that DIC compares favorably with other methods in terms of its ability to populate high spin states.

The preceding discussion shows that DIC can be a powerful tool for populating high spin states. It is clear that by using heavier projectiles it will be possible to reach spins up to the critical value at which the fragments become unstable with respect to fission (or α decay for lighter fragments). The amount of angular momentum transferred can furthermore be increased if one extends the detection of PLF's to more backward angles and then selects fragments from the sticking limit regime as discussed in Sec. III D.

In order to extract spectroscopic information for more highly excited states, it is clear that one needs to perform experiments which allow the collection of PLF-γ-γ events. Complete identification of the PLF would require the use of large solid-angle particle detectors, such as gas-filled chambers, capable of detecting DIC residues.

For most purposes, a simple Z identification should give sufficient selectivity of reaction channels. Another possibility, for experiments with more nearly equal projectile and target masses, is to simply measure the kinetic energies of both the PLF and TLF. In any case, it is highly desirable to have a measurement of the PLF scattering angle to allow Doppler-shift corrections.

In the present experiment, cluster transfers such as ^{6}He were observed, but no significant population of neutron-rich nuclei was observed. This was due primarily to the evaporation of neutrons from the residual TLF. Heavier projectiles with lower bombarding energies seem to be more effective for reaching high spin states with lower excitation energy and, thus, less neutron evaporation.

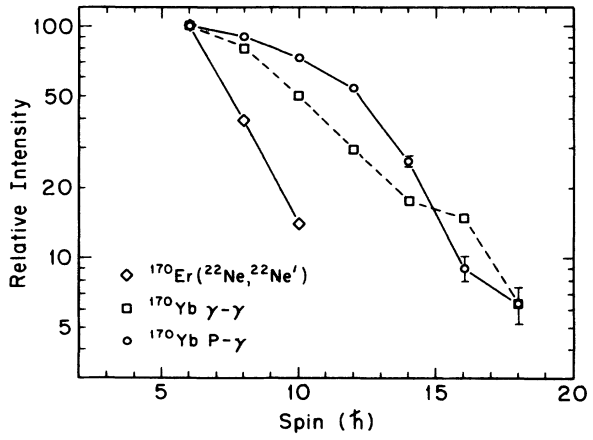

FIG. 18. Relative transition intensities of ^{170}Yb, for PLF-γ (circles) and γ-γ (squares) events. The intensities for inelastic excitation of the target are also included (diamonds).

IV. SUMMARY

The experimental arrangement resulted in an extensive characterization of each event and hence allowed the generation of data sets of high selectivity. The amount of orbital angular momentum transformed into intrinsic angular momentum was derived from the measured γ-ray multiplicities. It was found that quasi-elastic processes bring up to $\sim 25\hbar$ of angular momentum into the system and deep inelastic processes up to $40\hbar$. The measured

values were compared to the predictions of simple models, which described the gross features of data surprisingly well. Thus, these models will be very useful in the design of future experiments.

In the present experiment, discrete γ lines up to the $16^+ \rightarrow 14^+$ transition were identified in particle-γ coincidence data. For γ-γ coincidence data, the $20^+ \rightarrow 18^+$ transition was the highest observed. Using heavier projectiles, it should be possible to excite states with spins close to the critical value for fission. Thus deep inelastic collisions should provide an important new tool for high spin spectroscopy in regions of the table of isotopes that have hitherto been inaccessible to such studies.

The present experiment gave detailed information concerning reaction mechanisms. 56% to 88% of the exclusive cross section was due to binary processes while the remainder could be associated with breakup events. The observed ratio of the exclusive to inclusive cross sections was $\sim 50\%$, but this represents a lower limit since a considerable number of weak channels will be missed in any experiment that is based on γ-ray spectroscopy. The multiplicity distribution for the missing cross section could be determined. It is low by $\sim 15\%$ relative to that of the exclusive cross section, indicating that the missing events are associated with a smaller amount of intrinsic angular momentum.

ACKNOWLEDGMENTS

We are very much indebted to the computer group and the accelerator operations staff at the National Superconducting Cyclotron Laboratory at Michigan State University for their support. This work was supported by the National Science Foundation (NSF) under Grant No. PHY-86-12245 (MSU), by the NSF (University of Pittsburgh), and by the U.S. Department of Energy under Contract No. DE-AC05-84OR21400 with Martin Marietta Energy System Inc. (Oak Ridge National Laboratory).

[1]B. Herskind, J. Phys. **41**, 106 (1980).
[2]M. W. Guidry *et al.*, Phys. Lett. **163B**, 79 (1985).
[3]R. K. Bhowmik, J. van Driel, R. H. Siemssen, G. J. Balster, P. B. Goldhorn, S. Gonggrijp, Y. Iwasaki, R. V. F. Janssens, H. Sakai, K. Siwek-Wilczynska, W. A. Sterrenburg, and J. Wilczynski, Nucl. Phys. **A390**, 117 (1980).
[4]J. Wilczynski, K. Siwek-Wilczynska, J. van Driel, S. Gonggrijt, D. C. J. M. Hageman, R. V. F. Janssens, J. Lukasiak, and R. H. Siemssen, Phys. Rev. Lett. **45**, 606 (1980).
[5]J. Wilczynski, K. Siwek-Wilczynska, J. van Driel, S. Gonggrijt, D. C. J. M. Hageman, R. V. F. Janssens, J. Lukasiak, R. H. Siemssen, and S. Y. van der Werf, Nucl. Phys. **A373**, 109 (1982).
[6]C. P. M. Engelen, E. A. Bakkum, R. J. Meijer, and R. Kamermans, Nucl. Phys. **A457**, 375 (1986).
[7]M. Lefort and Ch. Ngo, Ann. Phys. (Paris) **3**, 5 (1978).
[8]J. B. Natowitz, M. N. Namboodiri, P. Kasiraj, R. Eggers, L. Adler, P. Gonthier, C. Cerruti, and T. Alleman, Phys. Rev. Lett. **40**, 751 (1978).
[9]H. Utsonomiya, E. C. Deci, R. A. Blue, L. H. Harwood, R. M. Ronningen, K. Siwek-Wilczynska, J. Wilczynski, and D. J. Morrissey, Phys. Rev. C **33**, 185 (1986).
[10]J. X. Saladin, IEEE Trans. Nucl. Sci. **NS-30**, 420 (1983).
[11]C. N. Knott, Ph.D. thesis, University of Pittsburgh, 1988.
[12]M. Jääskeläinen, D. G. Sarantites, R. Woodward, F. A. Dilmanian, J. T. Hood, R. Jääskeläinen, D. C. Hensley, M. L. Halbert, J. H. Barker, Nucl. Instrum. Methods **204**, 385 (1983).
[13]A. Gavron, Phys. Rev. C **21**, 230 (1980).
[14]D. G. Sarantites, J. H. Barker, M. L. Halbert, D. C. Hensley, R. A. Dayras, E. Eichler, N. R. Johnson, and S. A. Gronemeyer, Phys. Rev. C **14**, 2138 (1976).
[15]P. J. Siemens, J. P. Bondorf, D. H. E. Gross, and F. Dickman, Phys. Lett. **36B**, 24 (1971).
[16]C. F. Tsang, Phys. Scr. **10A**, 90 (1974).
[17]R. Bass, *Nuclear Reactions with Heavy Ions* (Springer-Verlag, New York, 1980).
[18]W. U. Schröder and J. R. Huizenga, *Treatise on Heavy-Ion Science* (Plenum, New York, 1984), Vol. 2.
[19]M. Lefort and Ch. Ngô, Ann. Phys. (Paris) **3**, 5 (1978).
[20]T. Tanabe, K. Ogino, Y. Kadota, K. Haga, T. Kitahara, and T. Shiba, Phys. Rev. C **26**, 524 (1982).
[21]H. Homeyer, M. Bürgel, M. Clover, Ch. Egelhaaf, H. Fuchs, A. Gamp, D. Kovar, and W. Rauch, Phys. Rev. C **26**, 1335 (1982).
[22]T. Shimoda, K. Katori, T. Fukuda, H. Ogata, S. Shimoura, M. Tanaka, and E. Takada, J. Phys. Soc. Jpn. **55**, 3021 (1986).
[23]W. Dünnweber, in *Nuclear Structure and Heavy-Ion Dynamics,* Proceedings of the International School of Physics "Enrico Fermi," Course LXXXVII, Varenna, 1982, edited by I. Moretto and R. A. Ricci (North-Holland, Amsterdam, 1984).
[24]S. Wald, S. B. Gazes, C. R. Albitson, Y. Chan, B. G. Harvey, M. J. Murphy, I. Tserruya, R. G. Stokstad, P. J. Countryman, K. van Bibber, and H. Homeyer, Phys. Rev. C **32**, 894 (1985).
[25]W. Nöremberg, in *Heavy Ion Collisions,* edited by R. Bock (North-Holland, Amsterdam, 1980), Vol. 2, pp. 3–43.
[26]Walker *et al.*, Phys. Lett. **86B**, 9 (1979).
[27]J. R. Cresswell, P. D. Forsyth, D. G. E. Martin, and R. C. Morgan, J. Phys. G **7**, 235 (1981).
[28]D. Ward, P. Colombani, I. Y. Lee, P. A. Butler, R. S. Simon, R. M. Diamond, and F. S. Stephens, Nucl. Phys. **A266**, 194 (1976).
[29]P. M. Walker, S. R. Faber, W. H. Bentley, R. M. Ronningen, and R. B. Firestone, Phys. Lett. **87B**, 339 (1979).

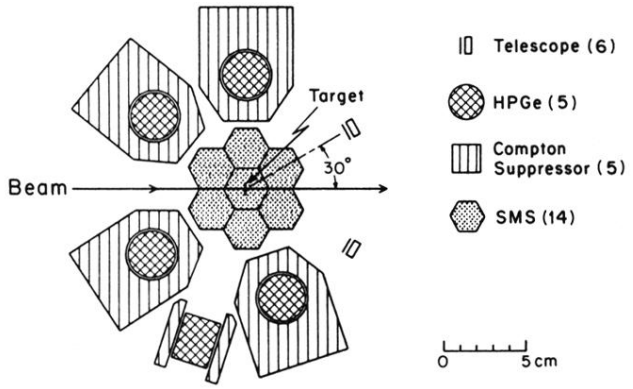

FIG. 1. Horizontal cross section of the apparatus showing the various types of detectors and their arrangement.